Heralded single-photon and correlated-photon-pair generation via spontaneous four-wave mixing in tapered optical fibers

A. A. Shukhin,[1,*] J. Keloth,[2] K. Hakuta,[2] and A. A. Kalachev[1]

[1]*Zavoisky Physical-Technical Institute, Kazan Scientific Center of the Russian Academy of Sciences, 10/7 Sibirsky Tract, Kazan 420029, Russia*

[2]*Center for Photonic Innovations, University of Electro-Communications, Chofu, Tokyo 182-8585, Japan*

(Received 14 October 2019; accepted 13 April 2020; published 11 May 2020)

We study the generation of frequency nondegenerate correlated photon pairs and heralded single photons via spontaneous four-wave mixing (SFWM) in a series of identical micro- or nanofibers (MNFs). Joint spectral intensity of the biphoton field generated at wavelengths of about 880 and 1310 nm has been measured under excitation by 100-ps laser pulses demonstrating good agreement with the theoretical prediction. The measured zero-time second-order autocorrelation function was about 0.2 when the emission rate of the heralded photons was of 4 Hz. The MNF-based source perfectly matches standard single-mode fibers, which makes it compatible with the existing fiber communication networks. In addition, SFWM observation in a series of identical MNFs allows for increasing the generation rate of single photons via spatial multiplexing.

DOI: 10.1103/PhysRevA.101.053822

I. INTRODUCTION

Currently, much attention is being paid to developing nonclassical light sources, such as those of single-photon and entangled two-photon states, which remains an important task in the field of quantum optical technologies [1,2]. One of the promising approaches to the problem is the use of nonlinear optical effects. Indeed, spontaneous parametric down-conversion and spontaneous four-wave mixing (SFWM) have been widely used for the generation of entangled photon pairs and heralded single photons [3]. In particular, significant experimental progress has been achieved in implementing SFWM-based fiber sources that perfectly match the existing fiber communication networks [4–12]. In this respect, tapered optical fibers or micro- or nanofibers (MNFs) seem to be very promising nonlinear materials [13–17] that have a number of unique features due to their small mode diameter, significant evanescent field, and small weight and size. In particular, MNFs can be used for optical sensing [18], observation of nonlinear optical effects at very low pump power level (below 10 nW) [19], manipulating single atoms [20], and for efficient coupling between light and matter [21]. The subwavelength diameter of MNFs allows one to construct miniature optical devices, which are characterized by small losses and low energy consumption, including miniature high-Q resonators [13]. Compared to the sources utilizing standard optical fibers, MNFs provide higher nonlinearity, which allows one to reduce the fiber length. In addition, the dispersion of a MNF can be tailored by controlling the fiber diameter, thereby separating spectra of SFWM and Raman scattering. At the same time, adiabatic fiber tapers are characterized by very small losses so that MNFs also perfectly match optical communication lines.

The generation of correlated two-photon and heralded single-photon states via SFWM in a MNF has been studied recently in [22–25]. Correlated photon pairs were also generated in highly nonlinear chalcogenide tapered microwires [26]. In the present work, we demonstrate a frequency nondegenerate correlated photon pair source and heralded single-photon generation based on SFWM in a MNF. Compared to the previous experiments, we have measured the joint spectral intensity (JSI) of the biphoton field and heralded autocorrelation histogram. In doing so, we observe SFWM in a series of identical MNFs, which can be used for increasing the generation rate of heralded single photons via spatial multiplexing. In addition, we calculated JSI using the models of an inhomogeneous micro- or nanofiber, thereby achieving good agreement between the theory and experiment.

II. MICRO- OR NANOFIBER FABRICATION

Subwavelength optical fibers with the cladding diameter less than $\sim$1 μm were made from the standard optical fibers [SMF-28, $d_{\text{core}}(\text{Ge}:\text{SiO}_2) = 10$ μm, $d_{\text{cladding}}(\text{SiO}_2) = 125$ μm] by using a heating and stretching method [14]. The MNF pulling setup is schematically shown in Fig. 1(a).

While tapering, the optical fiber is fixed on two moving translation stages and placed in front of a motionless flame of a burning O_2 and H_2 mixture. The movement of the translators consists of two types: synchronous displacement relative to the flame (swing) that determines heating zone and displacement in opposite directions (stretching) that determines fiber stretching distance and correspondingly the MNF region. These movements are determined by four parameters: swing speed, swing distance, stretching speed, and stretching distance so that a required adiabatic MNF profile can be

*anatoly.shukhin@mail.ru

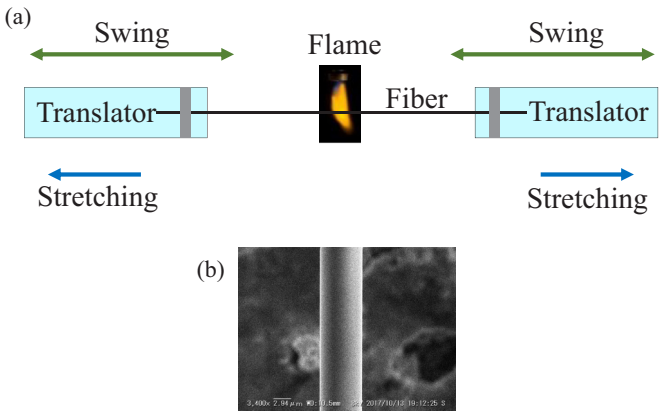

FIG. 1. Schematic representation of the MNF pulling setup (a) and electron microscope image of the fabricated MNF (b).

achieved [27] by adjusting them. As an example, an image of one of the fabricated MNFs is shown in Fig. 1(b). To control the MNF fabrication process, we measured the fiber transmission coefficient as a function of time while MNF pulling [Fig. 2(a)]. This dependence has three specific regions: (1) multimode losses region (50–70 s); (2) core mode cut-off region (70–290 s), and (3) single-mode losses region (290–350 s). The resulting transmission of all the fabricated MNFs at the wavelength of $\lambda = 680$ nm is measured to be $T \approx 99.6\%$.

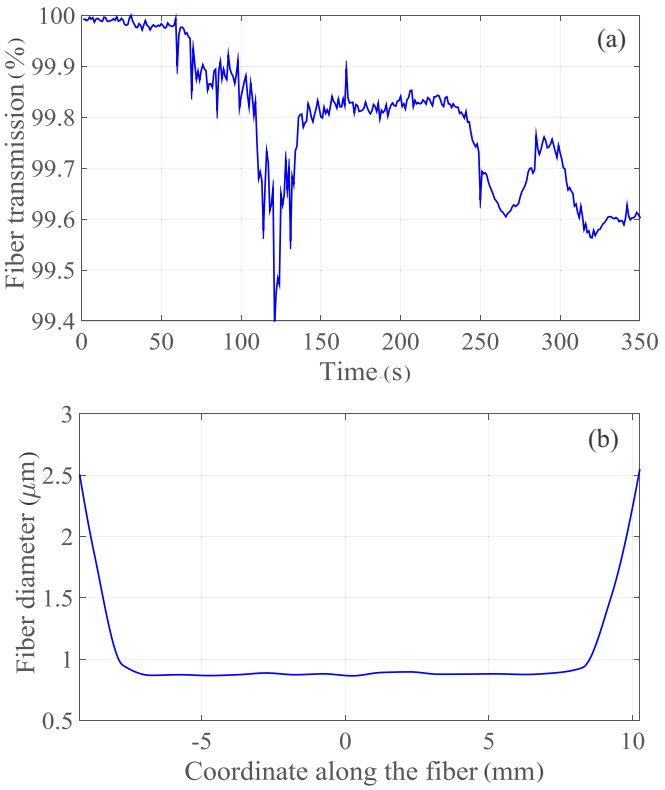

FIG. 2. Optical fiber transmission coefficient as a function of time while MNF pulling (a); the fiber diameter in the waist region as a function of the longitudinal coordinate (b).

Three regions in Fig. 2(a) are distinguished because they correspond to different regimes of the propagation of light and different composition of modes. The first region corresponds to multimode losses. As the diameter of the fiber decreases during the tapering process, modes of the fiber are no longer referred to as the core modes, but as cladding modes [28–30]. Fiber cladding now acts as the new core and the external air acts as the new cladding. The fiber in this region can support many modes [31,32]. As the fiber continues to stretch and the diameter decreases, the cladding modes gradually cut off until a few modes remain. That means that the adiabaticity of the tapering and the higher order cladding modes cut off are the reasons for the slight transmission drop in this region. The second region is the core mode cut-off region where the fundamental mode starts to propagate in the cladding of the fiber and not in the core. The behavior of the plot in this region allows us to understand how adiabatic the tapering part of fiber is. If there was a transmission drop in this region, then the tapering would not be adiabatic and we had to change the parameters of the pulling setup. But this is not the case here. The third region corresponds to single-mode losses. The transition drop in this region is caused by the presence of the dust in the air that surrounds the fiber and by the imperfections of the fiber preparation before pulling. Thus by measuring and analyzing the fiber transmittance as a function of time during the fiber tapering process, we can control the latter in many aspects, thereby producing micro- or nanofibers of high quality.

SFWM is a third-order optical nonlinear process, whereby the nonlinear interaction occasionally leads to the annihilation of two photons of the pump field and the simultaneous creation of two photons, which are usually called signal and idler, with different (nondegenerate regime) or the same (degenerate regime) frequencies. Due to the isotropic symmetry of the nonlinear medium, created photons have the same polarization as those of the pump. The process of SFWM satisfies the following energy and phase-matching conditions:

$$2\omega_p = \omega_s + \omega_i, \tag{1}$$

$$2\vec{k}_p = \vec{k}_s + \vec{k}_i, \tag{2}$$

where ω and $\vec{k}$ are the frequency and wave vector, respectively, of the pump (p), signal (s), and idler (i) photons. We used pump radiation at the central wavelength of 1062 nm. With such pump, it is possible to produce strongly nondegenerate photon pairs so that the wavelength of the idler photon falls into the telecommunication band while that of the signal photon proves to be in the spectral range where detection efficiency is high enough. For this purpose, to fulfill conditions (1) and (2), the MNF waist diameter should be about 900 nm. In addition, for high efficiency of SFWM to be achieved, MNFs with a long waist region are required. In the present work, a series of 11 MNFs has been fabricated with the waist diameter of $D \approx 890 \pm 12$ nm and the waist length of $L \approx 14$ mm. The result of MNF characterization by scanning electron microscopy is shown in Fig. 2(b). The fabricated MNFs have been sealed inside the plastic box to protect them from the dust.

III. SFWM IN AN OPTICAL MICRO- OR NANOFIBER

A. Theory

A two-photon (biphoton) state of SFWM field generated in a MNF can be calculated in the first-order perturbation theory of quantum mechanics [33]. Under this approach, the state vector of the biphoton field for a MNF of a variable cross section can be written as follows:

$$|\psi\rangle = |0\rangle + A\int F(\omega_s,\omega_i)a^{\dagger}_{m_sn_s}(\omega_s)a^{\dagger}_{m_in_i}(\omega_i)|0\rangle d\omega_s d\omega_s, \tag{3}$$

where $|0\rangle$ corresponds to the vacuum state of the electromagnetic field, A is a constant proportional to the nonlinearity of the fiber material, $a^{\dagger}_{mn}(\omega)$ is the photon creation operator in a fiber spatial mode with the distribution $u_{mn}(\rho)$, $\int |u(\rho)|^2 d^2\rho = 1$, $d^2\rho = dx\,dy$, and frequency ω,

$$F(\omega_s,\omega_i) = \mathcal{I}(\omega_s,\omega_i)\,\mathcal{J}(\omega_s,\omega_i) \tag{4}$$

is the joint spectral amplitude (JSA), which is proportional to the phase-matching function,

$$\mathcal{J}(\omega_s,\omega_i) = \sum_{q=1}^{N}\left[\mathrm{sinc}\left(\frac{\Delta k_q(\omega_s,\omega_i)l}{2}\right)\exp\left(\frac{i\Delta k_q(\omega_s,\omega_i)l}{2}\right)\times\exp\left(i\sum_{n=q+1}^{N}\Delta k_n(\omega_s,\omega_i)l\right)\eta^{q}_{m_pn_p,m_pn_p,m_sn_s,m_in_i}\right], \tag{5}$$

and the pump function, $\mathcal{I}(\omega_s,\omega_i)$, that has the form of convolution of the pump field spectral amplitude,

$$\mathcal{I}(\omega_s,\omega_i) = \int d\omega_p E_p(\omega_p)E(\omega_i+\omega_s-\omega_p). \tag{6}$$

Here, following [34], the MNF is divided by the N cross sections of the length l each, so that the total phase-matching function is the sum of those calculated for each cross section. In doing so,

$$\eta^{q}_{m_pn_p,m_pn_p,m_sn_s,m_in_i} = \int u_{m_pn_p}(\rho)u_{m_pn_p}(\rho)u^{*}_{m_sn_s}(\rho)u^{*}_{m_in_i}(\rho)\,d^2\rho \tag{7}$$

is the overlap integral between the four interacting modes that is calculated over the qth MNF cross section,

$$\Delta k_q = k_q(\omega_p) + k_q(\omega_i+\omega_s-\omega_p) - k_q(\omega_s) - k_q(\omega_i) \tag{8}$$

is the wave-vector mismatch for the qth MNF cross section, $k_q(\omega) = \omega n_{\mathrm{eff},q}(\omega)/c$, $n_{\mathrm{eff},q}(\omega)$ is the effective refractive index, and

$$E_p(\omega_p) = E_{p_0}\exp\left(-\frac{(\omega_p-\omega_{p_0})^2}{2\sigma^2}\right) \tag{9}$$

is the spectral amplitude of the pump field, which corresponds to a Gaussian pulse with the duration of $\tau_p = 2\sqrt{\ln 2}/\sigma$. Equation (5) is written for the case of a MNF with a variable waist diameter, which generalizes results obtained in [33] for a MNF of a constant diameter. It should be noted that each cross section is characterized by its own diameter, overlap integral, wave-vector mismatch, and additional phase [the second exponent in Eq. (5)] acquired by light due to the propagation through the rest of the cross sections. The latter is taken into account by the summation from the cross-section number $q+1$ to the cross-section number N in Eq. (5).

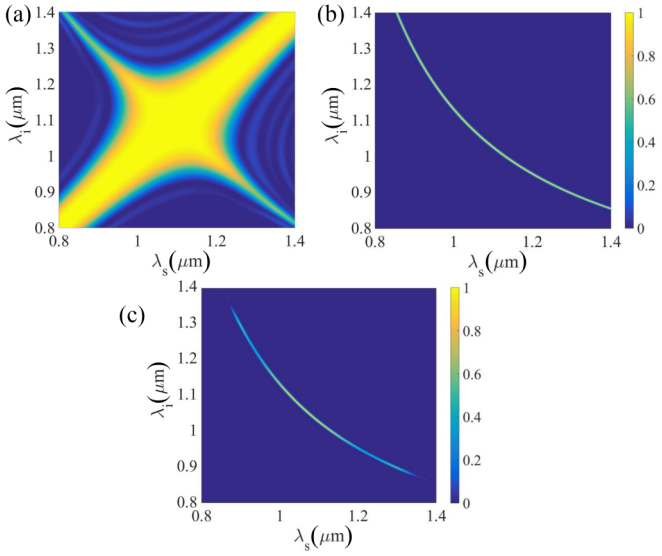

FIG. 3. Theoretically calculated phase-matching function (a), pump function (b), and joint spectral intensity (c) for the MNF whose profile is shown in Fig. 2(b).

Due to the small diameter of the MNF, all the interacting fields (pump, idler, and signal) correspond to the fundamental mode of the tapered fiber. The average value of the overlap integral (7) in our case is equal to 1.5×10^{12} m^{-2} for a MNF waist diameter of 890 nm, which is larger than that for a standard optical fiber by two orders of magnitude. The phase-matching function (5) is calculated taking into account the measured profile of the fabricated MNFs [Fig. 2(b)]. The squared absolute value of this function shown in Fig. 3(a) describes the probability density of the photon pair generation as a function of the wavelengths in the limit of an infinitely broad pump field. Figure 3(b) shows the spectral function (6) corresponding to the pump field. As such, we used the radiation of a pulsed laser consisting of the Fianium master oscillator and the ytterbium-doped fiber-based amplifier (central wavelength 1062 nm, pulse width 100 ps, pulse repetition rate 18 MHz). Since the pump pulses are not bandwidth limited, the spectral width of the pump field is about 2 nm in our case (instead of 10^{-3} nm for bandwidth-limited-100-ps pulses).

Multiplication of the spectral pump function and phase-matching function corresponds to the JSA of the biphoton field (5). The square of the module of this function (joint spectral intensity) is shown in Fig. 3(c). From this figure we can see that there is an opportunity to produce nondegenerate photon pairs, when the idler photons are generated in the telecommunication O band, while the signal ones are generated in the spectral range that is close to the visible light where detection efficiency is high enough.

Joint spectral intensity (JSI) reveals the most important spectral properties of the biphoton field. Particularly, besides the spectral width and central wavelength of the generated

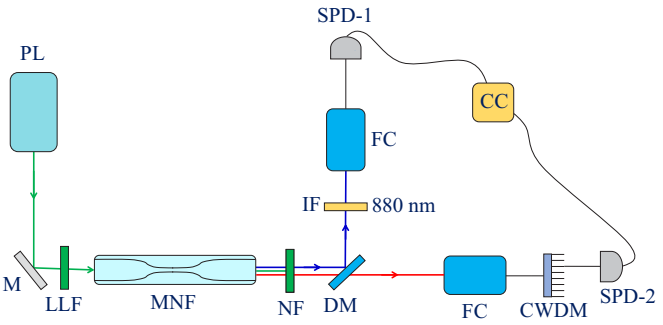

FIG. 4. Schematic of the experimental setup for studying SFWM in optical MNFs. PL is the pump laser, M is the mirror, LLF is the laser line filter, NF is the notch filter, DM is the dichroic mirror, IF is the interference filter, FC is the free space to fiber coupler, SPD is the single-photon detector, and CC is the coincidence counter.

photons, it allows one to analyze frequency correlations, which is important for heralded preparation of single-photon states [35,36]. Thus, measuring JSI for a fabricated MNF is an important step for characterization of the nonclassical light source.

B. Experiment

The experimental setup is schematically shown in Fig. 4.

The pump field passed through a laser line filter (LLF) and was focused with a lens into the tapered single-mode fibers. To cut off the pump field radiation after the fiber we used four notch filters (NFs) with 40 dB attenuation of each at the pump wavelength. The biphoton field generated in the MNF at the wavelengths of about 880 nm (signal) and 1310 nm (idler) was divided by using a dichroic mirror (DM). Idler photons have been filtered by using a coarse wavelength division multiplexing unit (CWDM) which has 18 bypass channels covering the spectral range from 1270 nm to 1610 nm with 20-nm bandwidth (FWHM) of each. After passing through one of these channels, idler photons went to the IR range single-photon detector SPD-2 (ID210, ID Quantique). Signal photons have been filtered by using an interference filter (IF) with the central wavelength of 880 nm and the bandwidth of 40 nm. After passing through the filter signal photons went to the visible range single-photon detector SPD-1 (SPCM-AQRH, Perkin-Elmer). The detection quantum efficiencies of SPD-1 and SPD-2 are about 40% and 12% at the signal and idler wavelengths, respectively. Signals from both SPDs have been compared on a coincidence counter (CC; id800, ID Quantique) with the time resolution of 81 ps. It should be noted that the total attenuation of the pump was equal to -220 dB in the signal channel and -200 dB in the idler channel.

The photocounts in both channels may be caused not only by SFWM, but also by Raman scattering of the pump field. To distinguish these contributions, we measured the single count rate in the signal channel as a function of the average pump power (Fig. 5) and fitted it by the second-order polynomial function $D + aP^2 + bP$. The quadratic term in this function corresponds to the contribution of the photons created via SFWM, while the linear one represents Raman

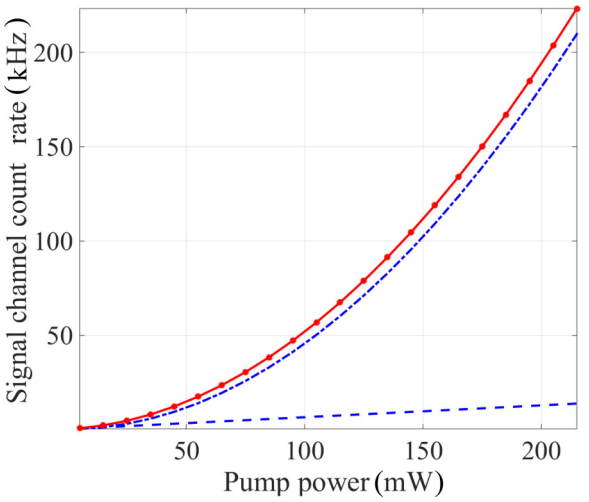

FIG. 5. Single count rate in the signal channel as a function of the average pump power. The solid line is the fitting of the experimental points by the second-order polynomial function $D + aP^2 + bP$; the dashed line and the dot-dashed curve are the linear ($b = 0.057$ kHz/mW) and quadratic ($a = 0.0043$ kHz/mW^2) terms of the fitting function, respectively. D is the dark count rate (400 Hz).

scattering [22,23]. The former proves to be close enough to the experimental points, which is evidence of the high contribution of the SFWM signal.

We also measured the single count rate in the idler channel as a function of the wavelength by using CWDM (Fig. 6). Two peaks of intensity are observed at the wavelengths of 1450 and 1610 nm. However, as will be shown below, the coincidence count rate demonstrates no signals for these CWDM channels, but only for the range of 1270–1350 nm. Moreover, the photocount rate in the idler channel depends linearly on the pump power, so that we can conclude that most of the photons in the idler channel appear due to the linear optical effects such as spontaneous Raman scattering. In particular, the intensity peak in the region of 1400–1450 nm is the fifth-order Stokes

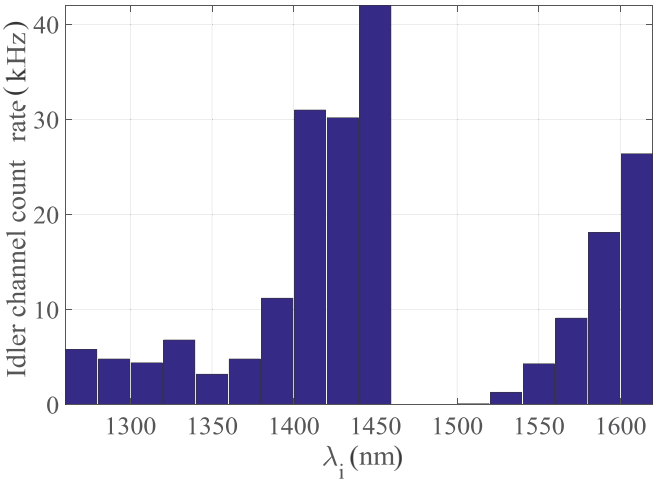

FIG. 6. Single count rate in the idler channel as a function of wavelength (after subtracting background noise, which is equal to 15.2 kHz). Average pump power is of 118 mW.

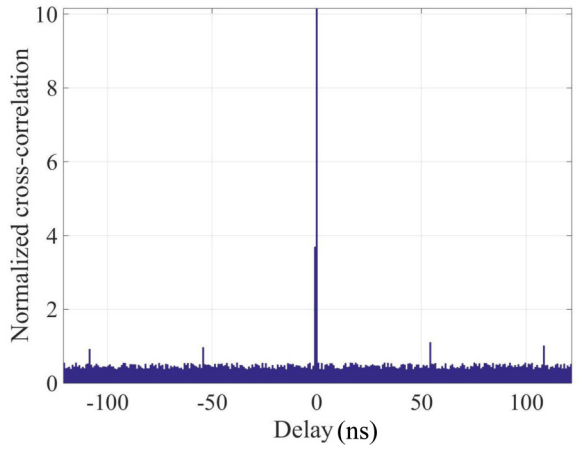

FIG. 7. Coincidence count rate as a function of time delay between the signal and idler photons. The width of each bar is 810 ps. The distance between the peaks corresponds to the time interval between the pump pulses and equals 54 ns. The average pump power is 118 mW.

line of Raman scattering in silica [37], while the peak around 1600 nm is interpreted as an unidentified line [22].

Figure 7 represents the normalized coincidence count rate as a function of the time delay between the signal and idler photons. The peak at the zero delay time corresponds to the strong temporal correlation between the photon detection events, which proves the two-photon nature of the generated light. The peak coincidence count rate and the accidental coincidence count rate as functions of the average pump power are shown in Fig. 8. The observed quadratic dependence for the peak coincidence count rate reveals high signal-to-noise ratio.

The use of the variable spectral filtering in the signal and idler channels allowed us to measure the JSI of the biphoton field. For spectral photon selection we used a diffraction grating (100 lines/mm) in the signal channel (instead of 880-nm

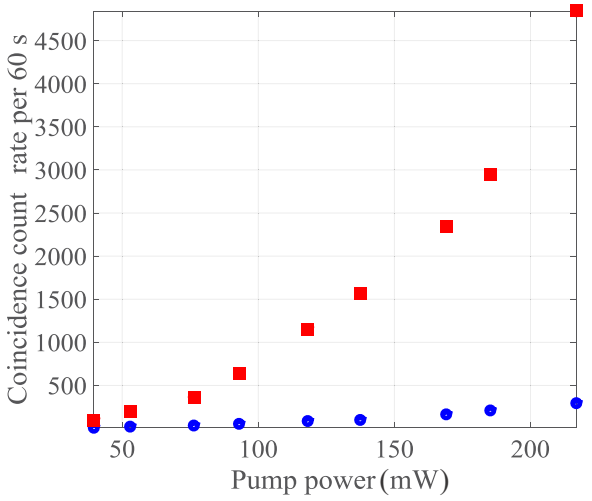

FIG. 8. Coincidence count rate (squares) and accidental coincidence count rate (dots) as functions of the average pump power. The CWDM channel central wavelength is 1310 nm.

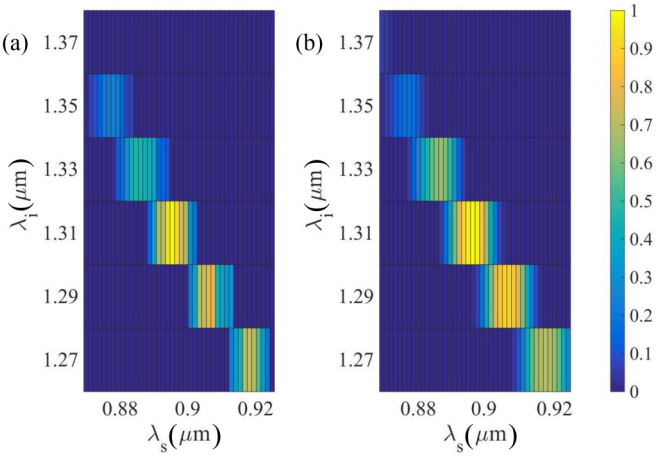

FIG. 9. Measured (a) and calculated (b) JSI for a given MNF. The average diameter of the MNF is estimated to be 900 nm.

interference filter) and the CWDM unit in the idler channel. By changing CWDM channels and rotating the diffraction grating we plotted the whole JSI function distribution in the experimentally accessible spectral range [Fig. 9(a)]. The resolution of the measurement was of 20 nm in the idler field and 1.5 nm in the signal field. Numerically calculated JSI demonstrates good agreement between the theory and experiment [Fig. 9(b)]. It is necessary to note that the JSI shown here is exactly the JSI shown previously in Fig. 3(c) that is zoomed on the region where the photon pairs are produced. Thus, it is the developed theory of SFWM in inhomogeneous tapered fibers that provides good agreement between the theory and experiment. We also measured the JSI in different micro- or nanofibers and got approximately the same position of its peak. Comparing the measured JSIs with the numerically calculated one allows us to estimate the diameter of the MNFs with accuracy of 3 nm. As a result, the waist diameter of all the MNFs lies within the 890 ± 12 nm region, as should be expected.

Following the papers [33,38], we calculated the photon pair conversion efficiency η for our MNFs (the probability of generation of a photon pair from two photons of the pump field sent to the nonlinear medium) and obtained $\eta = 7 \times 10^{-10}$ which gives the photon pair generation rate of $R = 3 \times 10^6$ pairs per second. The latter was found from the conversion efficiency by taking into account the number of photons in the pump pulse (2.67×10^8 at the average pump power of 118 mW) and the pump pulses repetition rate. Then by accounting for the losses in the setup (which include efficiencies of SPDs and losses on the optical elements per each channel, in total -17 dB), the observed photon flux turns out to be $R_{\text{observed}} = R\eta_i\eta_s \approx 60$ pairs per second (without spectral selection in the channels), which agrees well with the experimentally observed value of 40 photon pairs per second for the average pump power of 118 mW. Spectral filtering by using diffraction grating in the signal channel and CWDM unit in the idler channel reduces the observed photon flux down to four pairs per second.

The fact of simultaneous pair creation via SFWM, allows one to use the source of correlated photon pairs for

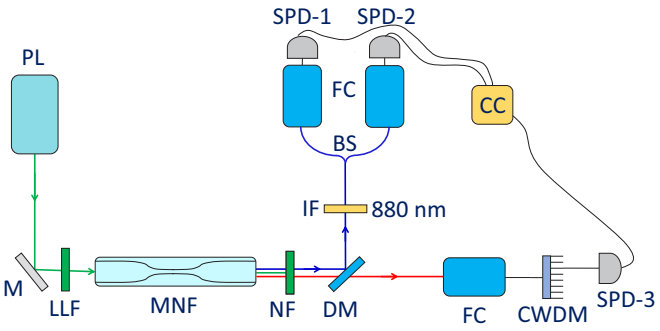

FIG. 10. Experimental setup for measuring heralded second-order autocorrelation. Here BS is a 50/50 (47/53) beam splitter at 850 nm (880 nm).

heralded single-photon generation, in which one photon from the pair is detected to herald the other. To study our source as a heralded single-photon one, we place a 50/50 beam splitter in the signal (heralded) channel (Fig. 10) and measured heralded autocorrelation histogram (Fig. 11). The heralded photodetection events are absolutely random and rare in comparison with the coincidence window (the latter was set to be of 810 ps for covering the jitter of the detection system). For this reason, the measuring of the second-order autocorrelation function, where the argument is the time delay between two heralded photons, is not possible. Instead, following the technique suggested in [39] and widely used for single-photon sources characterization [40–44], we measured the heralded autocorrelation histogram, where the argument is the number of heralding photons between the nearest heralded ones detected either by SPD-1 or SPD-2. This technique allows one to reduce the long time intervals between heralded photons but preserves all the probabilities of single-photon and many-photon events. In particular, the minimum value of such a histogram is equal to that of heralded autocorrelation function, i.e., it is an appropriate tool for characterizing so-called asynchronous heralded single-photon sources.

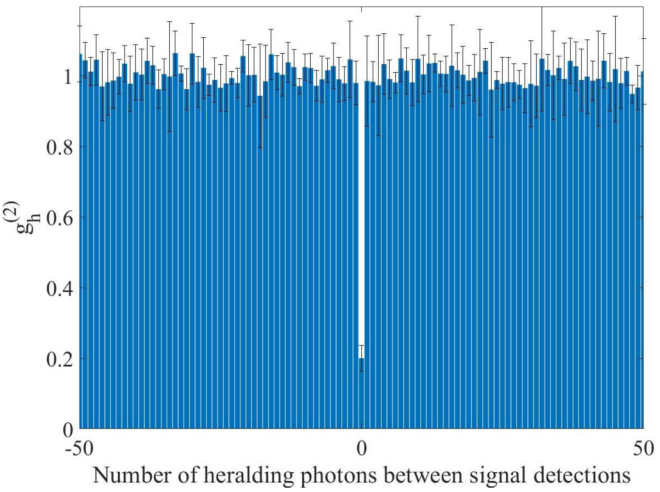

FIG. 11. Heralded autocorrelation histogram.

Experimentally, from the coincidence counting system we get the sequences $t1$, $t2$, and $t3$ of the time tags of the photons detected by SPD-1, SPD-2, and SPD-3, respectively. By analyzing these time tags, we obtained the histogram shown in Fig. 11. The antibunching drop at zero point indicates clearly the quantum behavior of the signal field and its single-photon statistics. For the average pump power of 118 mW and generation rate of 4 Hz, the value of zero-time second-order autocorrelation function (which is the same as the value of the zero-point autocorrelation histogram) is observed to be $g_h^{(2)}(0) \approx 0.2$. Each of the bars is obtained by accounting for all the photons detected within the coincidence window. The low generation rate and large deadtimes ($\approx$15 μs) led to about a week of running the experiment to accumulate a large enough number of threefold coincidences and present statistically significant results.

It should be noted that our experiment actually shows that picosecond pump pulses can also be used for studying SFWM in micro- or nanofibers (only femtosecond pump pulses were used in the previous experiments). In doing so, the photon generation rate proves to be high enough, and only losses in the signal and idler channels between the micro- or nanofiber and detectors reduce the counting rates significantly. However, these losses can be reduced to the same extent as for SFWM in usual fibers by optimizing the optical scheme of the setup.

IV. CONCLUSION

In this work, we have fabricated a bunch of identical 14-mm-long low-loss micro- or nanofibers and have studied spontaneous four-wave mixing in them by measuring the coincidence counting rate as a function of the pump power and the wavelength of the generated photons. The measured joint spectral intensity of the biphoton field agrees well with the theoretically expected distribution that is calculated considering the spatially inhomogeneous profile of the micro- or nanofibers. We also measured antibunching for the signal field, which is evidence of its single-photon nature. The high transmittance of the fabricated MNFs potentially allows one to significantly increase the photon pair conversion efficiency by making an all-fiber resonator using, e.g., two Bragg gratings enclosing the nanofiber waist [17]. Looking ahead, the source based on micro- or nanofibers would be more compact with respect to that based on usual fibers, which might be useful for implementing spatial multiplexing schemes.

ACKNOWLEDGMENTS

A.A.S. thanks the Center for Photonic Innovations, University of Electro-Communications for its hospitality. J.K. and K.H. thank the Japan Science and Technology Agency for the funding support through Strategic Innovation Program (Grant No. JPMJSV0918). The results of Sec. III were obtained within the government assignment for FRC Kazan Scientific Center of RAS.

[1] J. L. O'Brien, A. Furusawa, and J. Vučković, Nat. Photonics **3**, 687 (2009).

[2] F. Flamini, N. Spagnolo, and F. Sciarrino, Rep. Prog. Phys. **82**, 016001 (2019).

[3] M. D. Eisaman, J. Fan, A. Migdall, and S. V. Polyakov, Rev. Sci. Instrum. **82**, 071101 (2011).

[4] L. Wang, C. Hong, and S. Friberg, J. Opt. B: Quantum Semiclassical Opt. **3**, 346 (2001).

[5] J. E. Sharping, M. Fiorentino, and P. Kumar, Opt. Lett. **26**, 367 (2001).

[6] M. Fiorentino, P. L. Voss, J. E. Sharping, and P. Kumar, IEEE Photonics Technol. Lett. **14**, 983 (2002).

[7] H. Takesue and K. Inoue, Phys. Rev. A **70**, 031802(R) (2004).

[8] X. Li, P. L. Voss, J. E. Sharping, and P. Kumar, Phys. Rev. Lett. **94**, 053601 (2005).

[9] J. Rarity, J. Fulconis, J. Duligall, W. Wadsworth, and P. S. J. Russell, Opt. Express **13**, 534 (2005).

[10] J. Fan, A. Migdall, and L. Wang, Opt. Lett. **30**, 3368 (2005).

[11] Q. Lin, F. Yaman, and G. P. Agrawal, Opt. Lett. **31**, 1286 (2006).

[12] K. F. Lee, J. Chen, C. Liang, X. Li, P. L. Voss, and P. Kumar, Opt. Lett. **31**, 1905 (2006).

[13] G. Brambilla, J. Opt. **12**, 043001 (2010).

[14] L. Tong, F. Zi, X. Guo, and J. Lou, Opt. Commun. **285**, 4641 (2012).

[15] M. J. Morrissey, K. Deasy, M. Frawley, R. Kumar, E. Prel, L. Russell, V. G. Truong, and S. Nic Chormaic, Sensors **13**, 10449 (2013).

[16] V. I. Balykin, Usp. Fiz. Nauk **184**, 656 (2014).

[17] K. P. Nayak, M. Sadgrove, R. Yalla, F. Le Kien, and K. Hakuta, J. Opt. **20**, 073001 (2018).

[18] G. Y. Chen, M. Ding, T. Newson, and G. Brambilla, Open Opt. J. **7**, 32 (2013).

[19] S. M. Spillane, G. S. Pati, K. Salit, M. Hall, P. Kumar, R. G. Beausoleil, and M. S. Shahriar, Phys. Rev. Lett. **100**, 233602 (2008).

[20] F. Le Kien, V. I. Balykin, and K. Hakuta, Phys. Rev. A **70**, 063403 (2004).

[21] F. Le Kien, S. Dutta Gupta, V. I. Balykin, and K. Hakuta, Phys. Rev. A **72**, 049904(E) (2005).

[22] L. Cui, X. Li, C. Guo, Y. Li, Z. Xu, L. Wang, and W. Fang, Opt. Lett. **38**, 5063 (2013).

[23] J. Su, L. Cui, Y. Li, and X. Li, Chin. Opt. Lett. **16**, 041903 (2018).

[24] J.-H. Kim, Y. S. Ihn, Y.-H. Kim, and H. Shin, Opt. Lett. **44**, 447 (2019).

[25] E. Ortiz-Ricardo, C. Bertoni-Ocampo, Z. Ibarra-Borja, R. Ramirez-Alarcon, D. Cruz-Delgado, H. Cruz-Ramirez, K. Garay-Palmett, and A. Uren, Quantum Sci. Technol. **2**, 034015 (2017).

[26] E. Meyer-Scott, A. Dot, R. Ahmad, L. Li, M. Rochette, and T. Jennewein, Appl. Phys. Lett. **106**, 081111 (2015).

[27] J. Ward, A. Maimaiti, V. H. Le, and S. N. Chormaic, Rev. Sci. Instrum. **85**, 111501 (2014).

[28] A. Snyder, IEEE Trans. Microwave Theory Tech. **18**, 608 (1970).

[29] P. Clarricoats and K. Chan, Proc. Inst. Electr. Eng. **120**, 1371 (1973).

[30] P. Clarricoats, Prog. Opt. **14**, 327 (1977).

[31] L. C. Bobb, P. Shankar, and H. D. Krumboltz, J. Lightwave Technol. **8**, 1084 (1990).

[32] J. M. Corres, F. J. Arregui, and I. R. Matias, J. Lightwave Technol. **24**, 4329 (2006).

[33] K. Garay-Palmett, A. B. U'Ren, and R. Rangel-Rojo, Phys. Rev. A **82**, 043809 (2010).

[34] B. Katsenelenbaum, *The Theory of Irregular Waveguides with Slowly Varying Parameters* (USSR Academy of Sciences Publisher, Moscow, 1961), in Russian.

[35] P. J. Mosley, J. S. Lundeen, B. J. Smith, P. Wasylczyk, A. B. U'Ren, C. Silberhorn, and I. A. Walmsley, Phys. Rev. Lett. **100**, 133601 (2008).

[36] J. B. Spring, P. S. Salter, B. J. Metcalf, P. C. Humphreys, M. Moore, N. Thomas-Peter, M. Barbieri, X.-M. Jin, N. K. Langford, W. S. Kolthammer *et al.*, Opt. Express **21**, 13522 (2013).

[37] G. Agrawal, *Nonlinear Fiber Optics* (Academic, New York, 2012).

[38] K. Garay-Palmett, M. Corona, and A. U'Ren, Rev. Mex. Fis. S **57**, 6 (2011).

[39] S. Fasel, O. Alibart, S. Tanzilli, P. Baldi, A. Beveratos, N. Gisin, and H. Zbinden, New J. Phys. **6**, 163 (2004).

[40] D. Rieländer, A. Lenhard, M. Mazzera, and H. de Riedmatten, New J. Phys. **18**, 123013 (2016).

[41] A. Seri, D. Lago-Rivera, A. Lenhard, G. Corrielli, R. Osellame, M. Mazzera, and H. de Riedmatten, Phys. Rev. Lett. **123**, 080502 (2019).

[42] A. Seri, G. Corrielli, D. Lago-Rivera, A. Lenhard, H. de Riedmatten, R. Osellame, and M. Mazzera, Optica **5**, 934 (2018).

[43] A. Lenhard, J. Brito, M. Bock, C. Becher, and J. Eschner, Opt. Express **25**, 11187 (2017).

[44] M. Bock, A. Lenhard, C. Chunnilall, and C. Becher, Opt. Express **24**, 23992 (2016).